Molecular Dynamics Simulation and Experimental Fabrication of Nanoporous Graphene Membranes for Optimal Water Permeability in Reverse Osmosis Desalination

Apoorv Khandelwal[1,*]

[1]Tesla STEM High School, Redmond WA, 98053, USA
[*]Corresponding author: apoorv.khand@gmail.com

ABSTRACT

Nanoporous graphene membranes have the potential to solve the problem of a dwindling supply of fresh water that affects nearly half the world's population by enabling low cost, efficient desalination of seawater. Modern reverse osmosis desalination plants are expensive, environmentally disruptive and consume large amounts of energy. Nanoporous graphene has demonstrated to be a highly efficient and permeable membrane. LAMMPS molecular dynamics software was utilized on a 100,000 core-hour supercomputer allocation to model a graphene-based desalination system for thirty 10 nanosecond trials. Optimal water permeability of nanoporous graphene in reverse osmosis was determined to be $124.4 \, \mathrm{L \, cm^{-2} \, d^{-1} \, MPa^{-1}}$ at a 6.2% porosity for maximum mechanical stability by variation of five porosities in membranes with hydrogenated and hydroxylated group lined pores. This permeability is 1.85 times greater than in previous studies, 5,180 times common thin-film and 17.3 times ultrafiltration membranes. Nanopores in monolayer and bilayer graphene sheets were experimentally fabricated, after preperation of graphene membranes by transfer and defect-sealing with atomic layer deposition and interfacial polymerization. Gallium ion bombardment with oxidative etching and oxygen plasma etching were used to respectively create $0.4 \, \mathrm{nm}$ and $1 \, \mathrm{nm}$ pores at densities up to $1.2 \times 10^{13} \, \mathrm{pores \, cm^{-2}}$ and $4.8 \times 10^{12} \, \mathrm{pores \, cm^{-2}}$. Samples were characterized by electron microscopy and spectroscopy. Water transport measurements demonstrated experimentally improved permeabilities of graphene up to $50 \, \mathrm{L \, cm^{-2} \, d^{-1} \, MPa^{-1}}$, corroborating molecular dynamics theory at that density by 92%, over a $20 \, \mathrm{cm^2}$ area of nanoporous graphene for desalination, which is the largest to date.

Introduction

The global water crisis and issues of water scarcity severely impact much of the world's population, including 1.2 billion people that have absolutely no physical access to clean water[1] and 1.6 billion that lack economic access to it[1]. Although water forms 71% of the Earth's surface, 96.5% of it is contained in seas and oceans and another 1.7% is fresh water trapped in icecaps[2], inhibiting it from human use[1]. Sea level rise due to climate change will force another 500 million people into geographic scarcity within the next several decades[3]. Furthermore, many countries lack the infrastructure and budget necessary to provide clean water from available sources of sea and brackish water by desalination. Even regions that currently have access to freshwater reservoirs, such as aquifers and rivers, consume more water than can be replenished and will inevitably face the same chronic freshwater shortage that already burdens many other countries. In fact, the rate of water usage has been increasing at more than twice that of human population growth in the last century[4].

Desalination increases the amount of fresh water available to humans for use by allowing us to tap into the vast reserve of ocean water, rather than just the limited reserve of fresh water. Reverse osmosis (RO) membranes are currently the most widely used method of desalination in the world, implemented in nearly 80% of desalination plants and accounting for 44% of the desalination production capacity[2]. This approach uses polymer membranes to filter Na^+ and Cl^- ions of salt from pressurized seawater. Even though this method can produce around 250 million gallons of fresh water per day in industrial settings[2], it still has drawbacks in its high cost and energy consumption, which often limit its use in areas whose populations need water the most. Modern desalination plants are often disruptive to the environment and consume a large amount of energy, while producing fresh water at very slow rates. Commercial thin-film composite (TFC) membranes are very high in salt rejection, but are limited by low water permeability[5]. Furthermore, some TFC and polymer materials commonly used in filtration, including cellulose, polyamide and polysulfone[6,7], are poor in resistance to temperature, oxidants, strong acids or bases, and organic solvents[6–8].

Recent research has yielded four nanomembranes for reverse osmosis desalination with great potential for success[9].

Graphene oxide framework (GOF), carbon nanotubes (CN), graphyne (G^y), and nanoporous graphene (NPG) membranes all pose promising applications for improved desalination[10] with relatively similar salt rejection and water permeability rates. While the four novel and existing SRO membranes are all capable of achieving near perfect salt rejection rates, each novel method has a rate of water permeability two to three orders of magnitude greater than of TFC membranes, which perform at around $0.024\,L\,cm^{-2}\,d^{-1}\,MPa^{-1}$ and are ~100 nm in thickness[11]. Ultrafiltration membranes are the best in SRO and demonstrate a water permeability of $7.2\,L\,cm^{-2}\,d^{-1}\,MPa^{-1}$[11], but are still beaten by nanomembranes in filtration rates.

The material graphene has been found to filter water more quickly and with greater energy efficiency than current methods, including commercial seawater RO, after perforation with atomic-sized holes. This makes it significantly more cost effective and practical[12]. This novel NPG membrane is a two-dimensional, single-atom thick sheet of sp^2-bonded carbon[13] with high strength, flexibility and chemical inertness. NPG membranes demonstrate great results due to these factors[12–16] and their negligible thickness[17] of 0.34 nm[18], leading to lower required pressures for water flux. As water molecules are 0.28 nm in van der Waals diameter[19] and salt ions are 0.35 nm or greater[20], pores allow for water transport, but block the larger salt ions, and research shows that maximum pore diameter in nanoporous graphene can be ~0.6 nm for maintaining complete salt rejection[11]. Furthermore, selectivity of ionic passage is dependent not only on size exclusion, but also electrostatic interactions between aqueous, charged ions and pores[15,21]. NPG membranes with hydroxyl-lined pores have achieved the best balance of water permeability and salt rejection in simulations to date, with a permeability of ~$67.2\,L\,cm^{-2}\,d^{-1}\,MPa^{-1}$ and maintenance of 100% salt rejection[12]. The hydroxyl functional group ($-OH$) lining pores is hydrophilic and enhances flux across the membrane in comparison with the hydrophobic hydrogenated group ($-H$)[12] or F-N-terminated pores[9,22].

Nanoporous graphene membranes have been fabricated in rudimentary forms for applications of molecular separation[21]. Ultraviolet-induced oxidative etching of graphene can create pores allowing for selective gas transport, but at low density and large size distribution, preventing precise separation of molecules[14]. Focused electron beam irradiation can create controlled size pores, although these are too large to block salts and the method cannot scale to larger areas[23]. Ion bombardment via focused ion beam has been utilized to create isolated defects, which have been grown to desirably-sized ~0.4 nm pores by oxidative chemical etching and a density of 6×10^{12} pores cm^{-2}[13]. However, this approach permits ionic transport as a result of overlap among pores and grain boundaries. Oxygen plasma etching is a simpler approach that can produce regions of NPG with 100% salt rejection and permeability of ~$6\,L\,cm^{-2}\,d^{-1}\,MPa^{-1}$ by osmotic pressure[24]. This permeability greatly exceeds that of TFC membranes, but is still orders lesser than predicted by simulation and was achieved in an extremely limited area of $19.6\,\mu m^2$. Grain boundaries, intrinsic defects and tears outside this region would permit passage of salt ions.

In this investigation, I apply molecular dynamics (MD) to find the optimal structure of NPG for desalination based on effects of porosity on mechanical stability. Experimental nanoporous graphene membranes are fabricated at various porosities to validate findings and demonstrate capacity for nanofiltration and desalination in continuous and significantly larger areas of up to $20\,cm^2$. Graphene membranes are defect-sealed and pores are created by ion bombardment and oxygen plasma etching to demonstrate an experimentally increased permeability of ~$50\,L\,cm^{-2}\,d^{-1}\,MPa^{-1}$ and 100% salt rejection.

Molecular Dynamics Simulations

MD simulations (MDS) can measure and determine performances of nanomembranes in RO systems[25]. Thus, it can find optimal porosity in NPG, by varying density of constant size pores, with the goals of maximizing water permeability and maintaining adequate salt rejection for clean water production. I hypothesized that maximizing porosity in NPG will cause an increase in water permeability, but decrease in salt rejection due to pore deformation from applied pressures. Prior research has shown a baseline for desalination across NPG at both realistic and high applied pressures. However, whether the porosity of an overall membrane affects its permeability and selectivity is unknown and has been unexplored. Water permeability could be further optimized at an increased porosity to produce desalination performances several orders of magnitude greater than modern systems and improve upon previous investigations. Finding an optimal, yet realistically feasible, structure in NPG membranes is critical to maximizing their characteristic permeability and creating advances towards large-scale manufacture and implementation.

MD was utilized to model a standard RO system consisting of over 6,400 atoms and 8 atom types, each with differing interaction parameters, and to modify the porosity of a graphene membrane in its variations. Thirty 10 ns trials were simulated, three for each variation of porosity and functional pore lining.

Initial Conditions
The system in study modeled a graphene membrane on the z = 0 plane, between two pistons at z = -50 and 20. Boundaries were 3 nm on the x and y axes, 9 nm from -60 to 30 on the z-axis, and periodic in all directions. Regions of water were positioned between the membrane and pistons. The saltwater feed or upstream region beneath the membrane was ionized with Na$^+$ and Cl$^-$ particles. The fresh water permeate or downstream region above the membrane was composed of only H$_2$O molecules. The Visual Molecular Dynamics (VMD)[26] software generated these atomic geometry files, ionize the saltwater region, and produce

pristine graphene sheets with the Nanotube Builder tool. Bonds were created and regular and dihedral angles were added in VMD. The graphene membrane and pistons were all modeled parallel to the xy-plane as 3 nm x 3 nm sheets of carbon atoms; although, different interaction potentials were applied to the pistons than the membrane to prevent water adsorption. 1,300 water molecules and 12 of each Na^+ and Cl^- ions were placed on the feed region against 400 permeate side water molecules in every variation of the system. This initial presence of water in the permeate region prevented vacuum formation[11].

Porosity and functional pore linings were the manipulated variables in simulation trials. Porosity was increased by incrementing pore count from zero to five in each variation of hydrogenated and hydroxylated functional groups. Each hydrogenated pore, having a fixed open area of 0.23 nm^2, increased porosity by 2.56%. Hydroxylated pores of 0.28 nm^2 in open pore area incremented porosity by 3.11%. A pristine sheet was considered to have 0% porosity. Pores were manually introduced by replacing carbon atoms with $-H$ or $-OH$ functional groups using the Avogadro software. Pores for each functional lining were created of equal size by removing carbon atoms in a set radius from the center of a carbon hexagon. In hydroxyl-passivated pores, endings were alternated between $-OH$ and $-H$ to prevent steric interactions among neighboring groups.
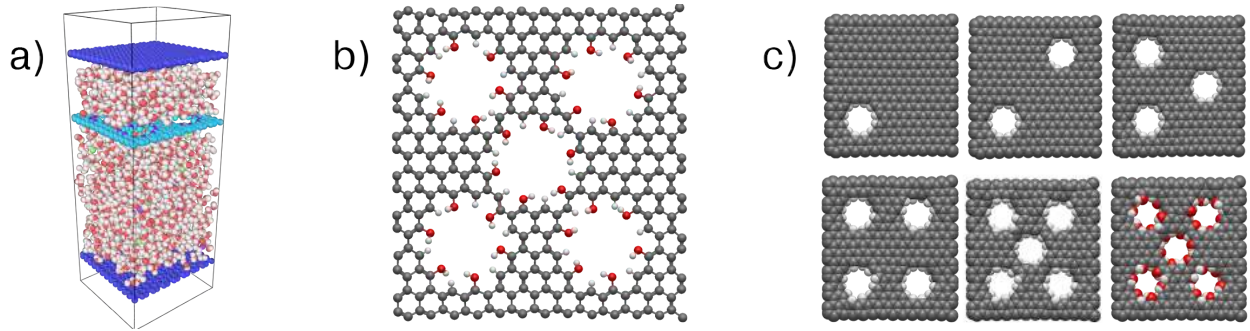
Figure 1. (a) Output of system composition from OVITO[27] demonstrating pressurized filtration across NPG. (b) Geometry file of 3 nm x 3 nm 5-pore hydroxylated graphene membrane, as displayed by Avogadro[28]. (c) Display of pore arrangements and functional pore linings in NPG membranes. Membrane on bottom-right consists of five hydroxylated pores, the remainder are of hydrogenated pores.

The simulation of study hybridized pairwise additive potentials among different atomic types, depending on function. All atomic species, including the graphene membrane and pistons[29–31], water bodies[32] and salt ions[33], were modeled by Lennard-Jones (LJ) and Coulombic parameters, with potentials given by equation (1), accounting for well depth (ε), distance between atoms (r), and van der Waals radius (σ).

$$V(r) = 4\varepsilon \left[\left(\frac{\sigma}{r} \right)^{12} - \left(\frac{\sigma}{r} \right)^6 \right] \tag{1}$$

Element	C (sp^2)[29]	C$_{COH}$[30]	H$_{COH}$[30]	O$_{COH}$[30]	C$_{CH}$[31]	H$_{CH}$[31]	H$_{H_2O}$[32]	O$_{H_2O}$[32]	Na$^+$[33]	Cl$^-$[33]
ε (kcal mol^{-1})	0.0859	0.0703	0	0.155	0.046	0.0301	0	0.16275	0.0117	0.1684
σ (Å)	3.3997	3.55	0	3.07	2.985	2.42	0	3.16435	5.1645	2.2589
q (e)	0	0.2	0.44	-0.64	-0.115	0.115	0.5242	-1.0484	-1	1

Table 1. Lennard-Jones parameters for interaction potentials used in simulations.

Interactions among different species were modeled with LJ and Lorentz-Berthelot mixing rules. The AIREBO potential was utilized at a scale factor of 3.0 to define the interactions of carbon and hydrogen atoms in the graphene, allowing for overall membrane deformation. To model AIREBO in a hydroxylated membrane and account for the oxygen atoms, all LJ parameters were removed from membrane atoms. A single carbon atom on the corner of the membrane was fixed in position to prevent the membrane from shifting, but still allow for deformation. Water did not flow around the membrane, as osmotic and applied pressures were exerted uniformly against both of its faces, keeping the membrane rigid. Osmotic pressure is additionally found to be higher closer to the membrane due to concentration polarization[34]. Of the many models representing interaction of water molecules, the TIP4P potential was selected, applying four bonding-sites to the molecules, including a massless partial charge behind the oxygen atom[35]. As the TIP4P model keeps intramolecular forces of H_2O molecules rigid, constraint algorithms must be applied, making it less computationally efficient than flexible models, such as SPC. Although this also demonstrates less computational efficiency than selecting a 3-site model, the TIP4P potential is important in this system to polarize, determine the

orientation of, and apply the electrostatic features of water. A simpler and more efficient model would be appropriate in a larger system and longer trial length. Salt ions were not polarized, as their transmembrane passage is primarily determined by applied pressures and not attractive forces[36].

Simulation

Each of the 30 simulation trials was run utilizing 4 Linux compute nodes, each with 12 dual-core 2.5 GHz processors, for a 45-hour period. Batch jobs were run simultaneously to generate trial results in a shorter period. The LAMMPS package[37] was selected as the MDS software, as it is effective for simulating inorganic systems and efficient in distributed computing.

Three 10 ns trials were simulated for each of the five values of porosity, ranging between 0% and 15.6%, and selected functional groups. Regions were defined in MD for pistons, feed water, permeate water, and the membrane, with appropriate charges set to water molecules and functional pore groups. Pair coefficients were applied to membrane atoms by AIREBO parameters and to the remaining type pairs by sigma and epsilon LJ values. Bond and angle coefficients of water molecules were also set based on the TIP4P potential. Appropriate atoms were then simulated by the Nosé–Hoover thermostat in an NVT ensemble with a damping constant of 100 ps and constant temperature of 300 K. Saltwater ions were set with randomized initial velocities according to the Gaussian distribution at this temperature, avoiding thermal shock and trial disruption. The systems initially underwent instantaneous static minimization, followed by equilibration for 40-60 ps, where pressure was not applied by either piston. Equilibration length was adjusted to modify initial geometry configurations, necessary to produce averages from system variation trials. Vertical forces were hence applied on both pistons towards the membrane at $1 \, \text{kcal} \, \text{mol}^{-1} \, \text{nm}^{-1}$ on the feed region and 1 atm of pressure against the permeate side. The feed piston force corresponded with a pressure of 32.11 MPa. This is larger than realistic applied pressures of ~5 MPa[2] and thus allows for greater accuracy in calculation of water permeability[38]. Each trial lasted for 10 000 000 fs over twenty million 0.5 fs time steps. All atomic trajectories were recorded per 500 fs. Thermodynamic data, including water and salt ion count in each region, were recorded every 1000 fs.

Results & Analysis

The Python-based Pizza.py package, a LAMMPS supplement, served as a wrapper for the VMD visualization tool and validated progression in the system during trials. Pizza.py provided the ability to write custom scripts, read thermodynamic output, and plot data in MATLAB. Water and salt molecule counts in the feed region were displayed over time steps for calculation of water flux and salt rejection. Accurate insights could be made for scaling nanoscale MD events to realistic results, as adequately low time steps between atomic position calculations were set, multiple trials were used, and pairwise interactions between atoms of interest were properly modeled.

The results of molecular dynamics simulations through variation of porosity and lining show that bare regions of NPG can be further optimized in structure to achieve permeability rates of $124.4 \, \text{L} \, \text{cm}^{-2} \, \text{d}^{-1} \, \text{MPa}^{-1}$, while maintaining adequate salt rejection, using hydroxylated pores of 0.598 nm in diameter at a density of $2.2 \times 10^{13} \, \text{pores} \, \text{cm}^{-2}$.

Pore Area & Porosity Calculations

Nanopore diameters were calculated using the standardized formula $d = 2\sqrt{A_{\text{pore}}/\pi}$, where d represents diameter and A_{pore} is the pore area, and were used as a measurement of pore size based upon open pore area.

Open pore areas were calculated by applying an integration function with AutoCAD software models of graphene nanopores resembled by van der Waals spheres. For the pores used in membrane geometries, $A_{\text{hydrog}} = 0.23 \, \text{nm}^2$ and $A_{\text{hydrox}} = 0.28 \, \text{nm}^2$. These areas were approximately 0.6 nm in diameter, meeting the criteria for adequate salt rejection by individual pores[39]. Porosity is the percentage of total pore area out of membrane area and is proportional to number of pores. In the formula for porosity $p = n \cdot A_{\text{p}} \cdot 100\%/A_{\text{g}}$, A_p (nm) is the value for area of either a single hydrogenated or hydroxylated pore with n pores and a constant membrane area A_g of $9 \, \text{nm}^2$.

Transmembrane Pressure Calculation

Transmembrane pressure was calculated from a force constant in the simulation with which the solid piston pressed against the molecules in the feed region. This variable, expressed by LAMMPS in $\text{kcal} \, \text{Å}^{-1} \, \text{mol}^{-1}$, was converted to the pressure in MPa by dimensional analysis and accounting for the $900 \, \text{Å}^2$ area of the 416 carbon atom membrane. The final value of pressure, used in the permeability calculations, was found to be 32.0 MPa after factoring in the opposing pressure of 1 atm from the permeate piston. Osmotic pressure (Π) of the feed region was 2.00 MPa, found from the van'tHoff equation ($\Pi = iMRT$) and as [NaCl] = 0.443 M.

Salt Rejection Rates

Salt rejection is the percentage of salt ions remaining in the feed region at the end of trials and after half the initially present water molecules have been filtered. As the standard criteria for fresh water is to contain less than $1000 \, \text{mg} \, \text{L}^{-1}$ of salts or total dissolved solids (TDS)[2], the threshold for minimum salt rejection is 99.1%. The trials demonstrate that porosities less than

5.11% in hydrogenated pore and 6.22% in hydroxylated pore membranes meet this requirement for salt rejection. Thus, the maximum feasible number of pores in 9 nm^2 NPG, as studied here, is two. The results of all trials with greater porosity show a drop in salt rejection, even to 72.2% in the case of five hydroxylated pores per unit cell, which is much lesser than the absolute threshold for salt rejection, and thus indicate a drop in mechanical stability.
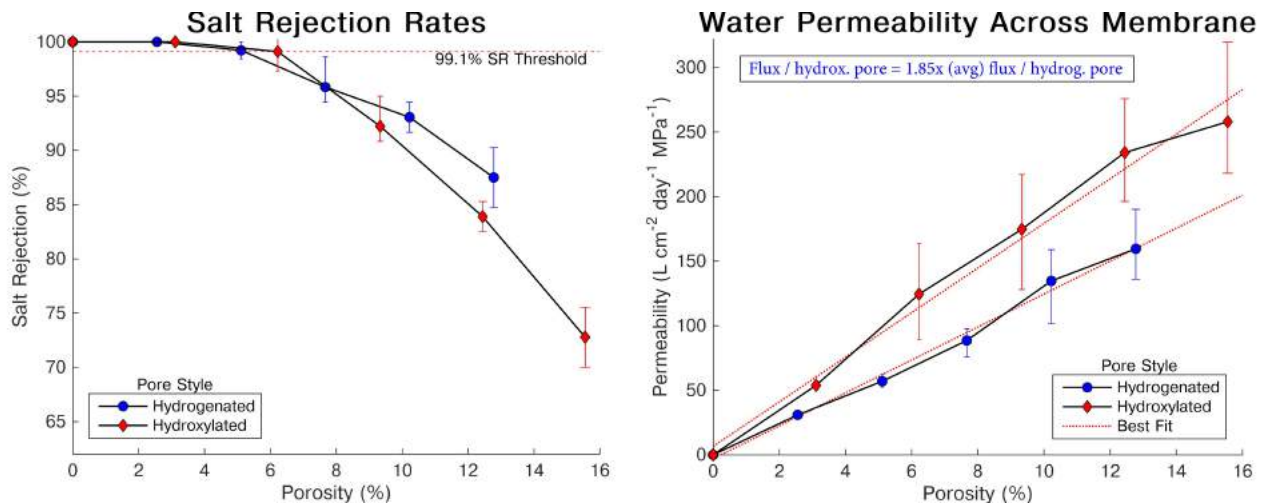
Water Flux & Permeability

Increase in porosity of a nanoporous graphene membrane will result in a proportional increase in its water flux and permeability. Flux was calculated at the time when half of the water molecules had been filtered from the feed region to permeate region, at which point there was no further increase in volume of permeate water. Pressure difference and osmotic pressure of seawater were taken into account for calculation of water permeability. The specific permeability values to this system were found to be linearly and directly proportional to flux with a coefficient of 1.004.

At the ideal structure of NPG, as found by salt rejection results, of 6.22% porosity with hydroxylated pores, membranes are able to filter water with a permeability of $124.4 \, \mathrm{L \, cm^{-2} \, d^{-1} \, MPa^{-1}}$.
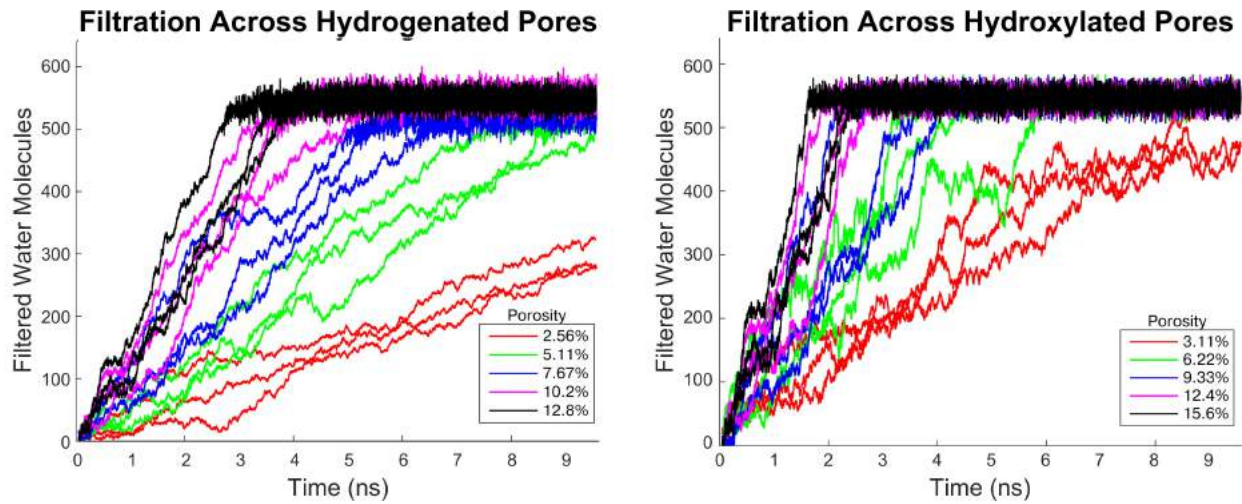
Figure 2. Results of water filtration versus porosity in 15 trials across each hydrogenated and hydroxylated NPG membranes.

Figure 3. Average values of water permeability and salt rejection against porosity in hydroxylated and hydrogenated graphene trials.

Large-scale Simulations

Three extended MD simulations were run using the optimal structure of NPG, as determined from the thirty prior trials. In this extended system, 18 equidistantly-spaced hydroxylated 0.6 nm pores were introduced across a 9 nm x 9 nm NPG membrane.

This system held the same thermodynamic conditions and interaction potentials as previously mentioned. The initial feed region contained 11,700 water molecules and permeate region contained 3,600 water molecules. 216 salt ions were initially present in the feed region, which was at the same concentration as in prior trials. Each of the extended trials lasted for 40 ns with a 0.5 fs time step. Equilibrium lengths of 50 ps, 100 ps and 150 ps were selected. A realistic transmembrane pressure of 5.0 MPa was applied towards the permeate region. By 27.5 ns of extended simulations, around 5,900 water molecules, or half the feed body, had filtered across the membrane and the permeate volume had stabilized. The average permeability of the membranes was thus found to be 119.5 $L\,cm^{-2}\,d^{-1}\,MPa^{-1}$, matching results of varied trials by 96%. An average and adequate salt rejection rate of 99.2% was found across the membranes by the end of trials.

Experimental Fabrication

Laboratory-scale nanoporous graphene membranes were experimentally fabricated to test for performance in desalination and compare with computational results. Low-pressure chemical vapor deposition (LPCVD) grown monolayer graphene sheets on copper foil (Graphenea Inc.) were transferred to polycarbonate track etch membrane (PCTEM) and silicon (Si/SiO_2) wafer substrates. Monolayer graphene was additionally purchased on 3 mm gold Quantifoil Holey Carbon TEM grids with 2 μm holes (Graphenea Inc.). However, the graphene sheets are only grown with ˜95% coverage. Intrinsic defects and grain boundaries of ˜10 nm formed during growth were sealed by atomic layer deposition (ALD). 100-200nm tears that formed during transfer were sealed via interfacial polymerization (IP). Two methods were used to create nanopores in graphene with structures similar to desired computational findings: ion bombardment, followed by oxidative etching, and reactive ion etching (RIE) by oxygen plasma. Resultant NPG samples were characterized by scanning electron microscopy (SEM), transmission electron microscopy (TEM), Raman spectroscopy and x-ray photoelectron spectroscopy (XPS). Diffusion measurements were carried out to determine water permeability and salt rejection of membranes.

To minimize surface contaminants, all glassware were cleaned by ultrasonication with acetone and rinsing with isopropyl alcohol. During graphene transfer, glass slides were silinated with vapor-phase chlorotrimethylsilane (Sigma-Aldrich) for 10 min to decrease surface energy and prevent adhesion. Ammonium persulfate (0.66 M in ethanol; $(NH_4)_2S_2O_8$; APS; Sigma-Aldrich) was used as a copper etchant during transfer, due to the following dissolution reaction between persulfate and copper.

$$Cu_{(s)} + S_2O_8{}^{2-}{}_{(aq)} \longrightarrow CuSO_{4(aq)} + SO_4{}^{2-}{}_{(aq)} \tag{2}$$

Sample Preparation

Twenty-four monolayer 1 cm x 1 cm graphene sheets were transferred from copper foil (Graphenea Inc.) onto non-PVP coated PCTEM with 200 nm pores (Sterlitech). Before transfer, PCTEM were soaked in didecylamine (60 $mmol\,L^{-1}$ in ethanol; Sigma-Aldrich) for 60 minutes and rinsed thrice on shaker plates with ethanol for 20 minutes to ensure consistent hydrophobicity and a dry interface between PCTEM and graphene. Backside graphene was removed by floating copper foils in APS for 7 min. Their graphene-faces were conformed unto PCTEM by light pressure and copper was removed by etching in the APS solution for 75 min. The PCTEM were left adhered with graphene and were rinsed in water and ethanol baths before air-drying. ˜92% of transfer attempts to PCTEM were successful.

Four bilayer graphene samples were fabricated by repeating the transfer method with graphene on copper unto four of the PCTEM-supported graphene sheets. Between conformation and etching, the graphene on copper conformed to PCTEM-supported graphene was placed in a 140 °C oven for 10 min to allow π-bond interaction between graphene layers.

Monolayer graphene was transferred onto nine polished 1 cm x 1 cm Si/SiO_2 wafers (Graphene Supermarket) by spin coating polycarbonate (1.5 wt%; PC) in chloroform onto graphene on copper. Copper was subsequently etched and remnants of samples were placed on the silicon wafers to air dry overnight. Polycarbonate was then removed by submersion in chloroform.
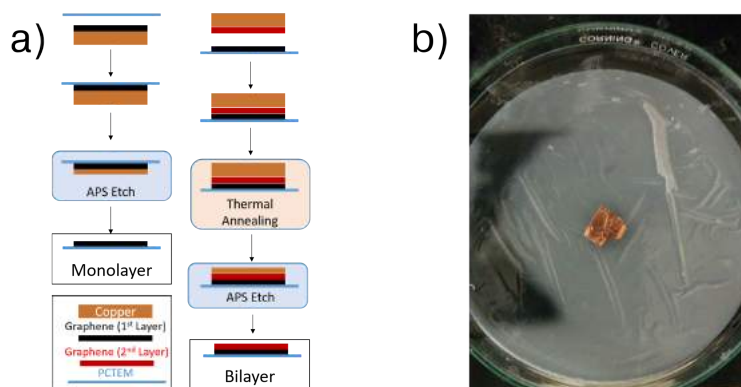
Figure 4. (a) Schema of monolayer and bilayer graphene transfer to PCTEM. (b) Photograph of graphene on copper conformed to PCTEM during etch.

Atomic layer deposition of hafnium oxide (HfO_2) was used to seal intrinsic defects and grain boundaries in graphene on PCTEM and TEM grids. This process was carried out with a Savannah S200 system (Ultratech/CNT). The chamber was initially purged with N_2 gas for 40 min and cycled 20 times with HfO_2. Forty cycles of deposition were then run at $130\,°C$ and $400\,mTorr$. Each cycle included a $0.025\,s$ H_2O pulse, $70\,s$ delay and $0.3\,s$ pulse of the tetrakis(dimethylamido)hafnium(IV) (TEMAH) precursor. The N_2 gas flowrate was increased from $20\,sccm$ to $30\,sccm$ during the delay to remove precursor particles outside defect regions. A $6.13\,nm$ layer of HfO_2 was deposited, found from ellipsometry using a Woollam M44 spectrometer on a bare Si/SiO_2 wafer that underwent deposition.
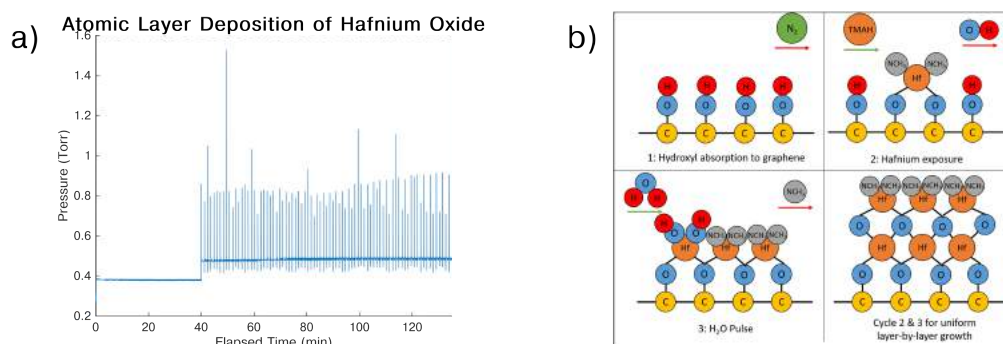
Figure 5. (a) Pressure cycles during hafnium oxide ALD. Low pressure until 40 minutes indicates nitrogen purge and spikes indicate pulses of precursor and H_2O. (b) Diagram of ALD cycles. Hafnium precursor and H_2O pulses are deposited sequentially to terminate all reactive sites on the substrate. This results in self-limiting and uniform growth of thin-films.

Nylon-6,6 was grown to seal the larger tears in graphene on PCTEM via unstirred IP for 60 min between hexamethylenediamine (98%; HMDA; Sigma-Aldrich) and adipoyl chloride (98%; APC; Sigma-Aldrich). A jacketed 5 mL Franz cell with 9 mm orifice (Permegear Inc.) was filled with HMDA (25 mg in water), adjusted to a pH of 9 by sodium bicarbonate. PCTEM were clamped graphene-side down between cell chambers and the topside was filled with APC ($5\,mg\,mL^{-1}$). After each reaction, the topside chamber was rinsed with hexane and ethanol before the PCTEM was removed to be washed thrice in ethanol baths and air-dried. At this point, 96% of original defect areas in graphene were sealed, as measured by diffusion experiments. Equation (3) represents the respective reaction between solutions of HMDA and APC monomers to form nylon polymers and HCl.

$$\text{n } NH_2(CH_2)_6NH_{2(aq)} + \text{n } ClCO(CH_2)_4COCl_{(aq)} \longrightarrow \text{n } NH(CH_2)_6NHCO(CH_2)_4CO_{(aq)} + 2\text{n } HCl_{(aq)} \tag{3}$$

Nanopore fabrication
Nanopores were introduced into graphene sheets on PCTEM, Si/SiO_2 wafers and TEM grids with two approaches. The first involved bombarding graphene surface with gallium ions to create defects, followed by etching samples in an oxidative solution to grow pores. The second approach applies short-term exposure of graphene to oxygen plasma to form pores.

Gallium Ion Bombardment & Oxidative Etching

A FEI Helios Nanolab 600 DualBeam focused ion beam (FIB) was used to bombard samples with gallium ions. For each exposed sample, the entire graphene area was bombarded. The $1 \, cm^2$ area on PCTEM and silicon wafers was divided over twenty windows and the $0.07 \, cm^2$ TEM grid area was divided into four windows. Each bombardment window had an area A_b of $0.055 \, cm^2$. The ion beam was applied at a 1.6 nA current, 8 kV acceleration voltage and 52° angle of incidence with a $1 \, \mu s \, pixel^{-1}$ dwell time and 4096 x 3536 pixel resolution. ~85% of impact sites from FIB were probabilistically expected to produce basal plane defects[40]. The bombardment density (n) was 1.6×10^{12} ions cm^{-2} (2 scans per window) for 3 monolayer PCTEM, 2 silicon wafers and 2 TEM grids. For 3 monolayer and 2 bilayer PCTEM, 2 silicon wafers and 2 TEM grids, $n = 3.2 \times 10^{12}$ ions cm^{-2} (4 scans per window). For 2 monolayer and 2 bilayer PCTEM, $n = 3.8 \times 10^{13}$ ions cm^{-2} (48 scans per window). Each scan lasted 13.5 s. Bombardment of each $1 \, cm^2$ area respectively took 0.15, 0.30 or 3.6 h for $n = 1.6 \times 10^{12}$, 3.2×10^{12} or 3.8×10^{13} ions cm^{-2}, as total exposure time T was calculated by equation (4).

$$T = \frac{n \cdot A_b \cdot i}{3e^-} \tag{4}$$

FIB bombarded samples on all substrates were floated graphene-side down in a solution of 1.875 mM KmNO$_4$ in 6.25% H$_2$SO$_4$ for 60 min. After this in situ oxidative etch, samples were removed and rinsed in two water baths for 10 min each. Through this process, 58.3% of impact sites created by FIB were expected to be grown into 0.4 ± 0.2 nm pores[13].

Oxygen Plasma Etching

The Vision RIE (Plasma-Therm AV) and the March CS-1701 RIE (Nordson Corp.) were used to etch pores into graphene sheets with O$_2$ plasma. These plasma cleaners were operated at 20 W RF power in a high vacuum chamber under a pure oxygen flow of 500 mTorr. 4 monolayer and 2 bilayer PCTEM, 2 silicon wafers and 2 TEM grids were exposed for 2 sec. 2 monolayer and 2 bilayer PCTEM, 2 silicon wafers and 2 TEM grids were exposed for 4 sec. Pore size and density both grow with increased exposure time[24]. With these configurations, ~1 nm pores were fabricated in the graphene samples. These are larger than the theoretical limit to pore size by desalination, but prior studies demonstrate nearly 100% salt rejection through pores of this size in microscopic areas of suspended graphene[24]. Pore density n (pores cm^{-2}) was estimated by equation (5) based on two empirical equations[41,42] and applied prior findings to predictively determine exposure times for desired n. This formula uses Raman spectroscopy at an excitation energy E_L (eV) and its resultant intensities of G and D bands, respectively I_G and I_D. 2 s exposures showed an I_D/I_G ratio of 1.72[24] and were predicted to induce 2.8×10^{12} pores cm^{-2}, while 4 s exposures demonstrated an I_D/I_G ratio of 1.91[24] and were predicted to grow 3.5×10^{12} pores cm^{-2}. Pore densities with this method were limited to these values, as larger exposure time would also grow pores to inadequate sizes.

$$n = \frac{4 \times 10^{14}}{(\frac{560}{E_L^4} + \frac{40.9}{E_L} - 12.9)^2} \cdot (\frac{I_D}{I_G})^2 \tag{5}$$

Scanning Electron Microscopy

Images of graphene on all substrates were taken during the FIB bombardment using the SEM column of the dual-beam microscope. When operating in field-free mode, the beam had a 5.00 kV acceleration voltage and current of 0.34 nA. SEM immersion mode was typically used at 2.00 kV and current of 86 pA when imaging areas less than 10 μm in width. All SEM images were taken at a 4096 x 3536 pixel resolution with a $1 \, \mu s \, pixel^{-1}$ dwell time.
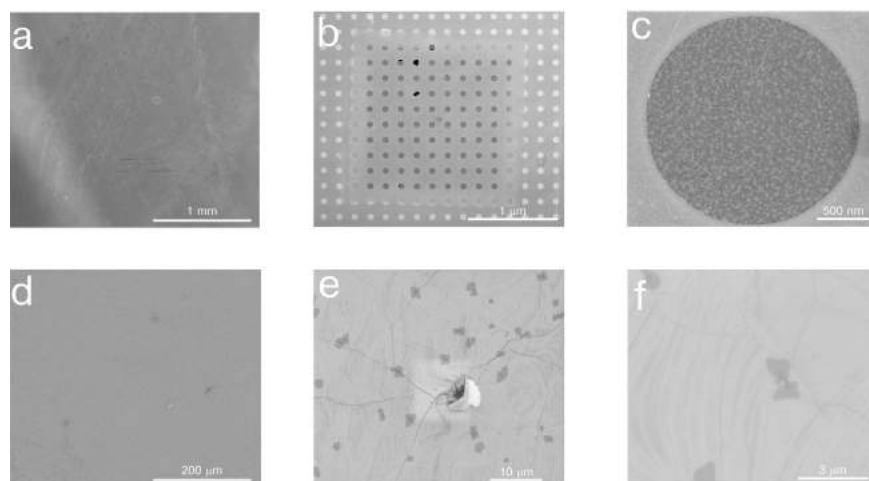
Figure 6. SEM images of graphene on PCTEM (a), TEM grids (b-c) and silicon wafers (d-f). Grain boundaries and intrinsic defects can be seen on silicon wafer substrates that were untreated by ALD or IP. These cannot be found on the treated PCTEM, although wrinkles from transfer can be, and TEM grids. Image (b) shows few tears in suspended graphene, due to the delicate nature of holey TEM grids, although tears are not present in PCTEM.

Transmission Electron Microscopy

The FEI Titan 80-200 TEM and FEI Titan 80-300 TEM were used to image all TEM grid samples. Both imgaging methods of Scanning Transmission Electron Microscopy (STEM) and TEM were used, producing images with varying contrast to detect pores. Both TEM and STEM were operated at 80 keV, in order to prevent damage to graphene during imaging, although resolution was sacrificed and long exposures caused additional pore growth. The STEM beam used a convergence semi-angle of 18 mrad and half-angle annular dark field detector at 100 mrad. For each sample, twenty 20 000 nm^2 images were taken by the TEM. ImageJ software was used to sharpen and improve pore distinction by a low-pass smoothing function. An image processing algorithm was written in Java to stitch images together and detect pore edges with the Canny Edge Detector plugin for ImageJ. Pores were then counted and their areas were measured with ImageJ's particle analyzer tool by this automated method.
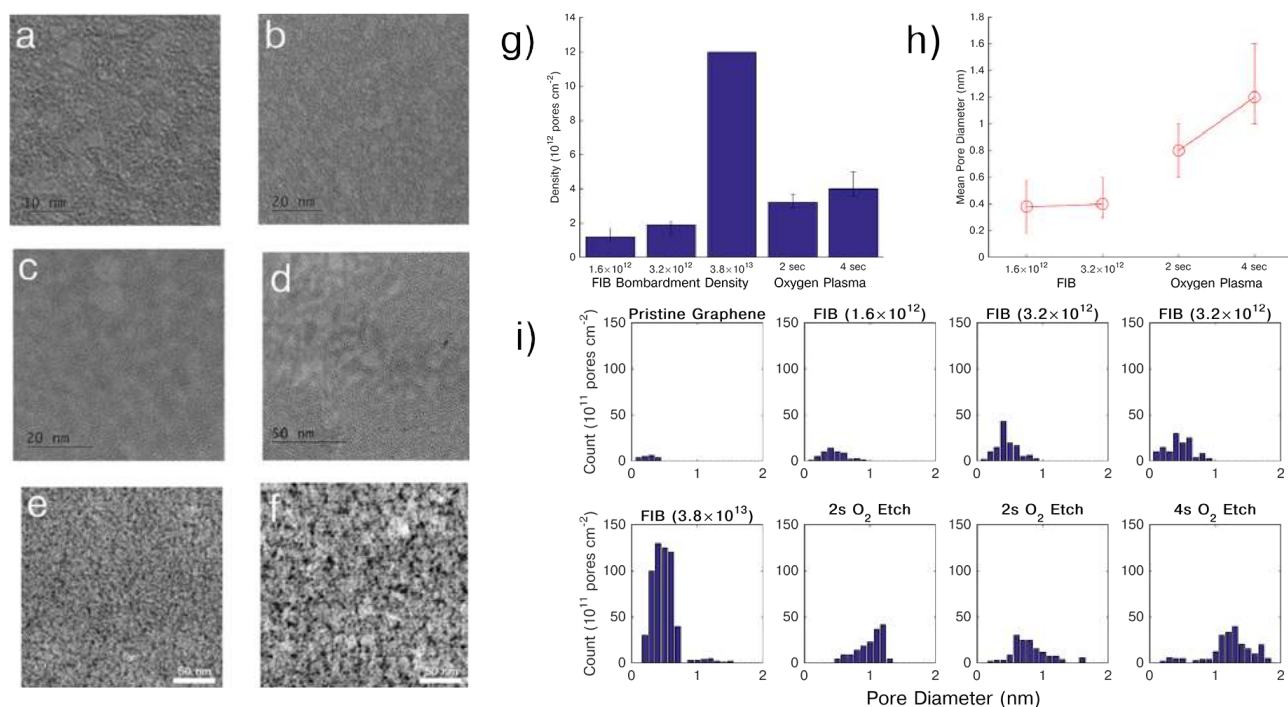
Figure 7. (a-f) STEM and TEM images of FIB bombarded (a-c) and plasma etched (d-f) graphene samples. Sub-nm pores can be seen, especially with the STEM dark field detector in (e-f). (g-h) Graphs of average pore density and diameter by pore growth method of imaged TEM grids. (i) Graphs of pore distributions by size for each imaged sample.

Raman Spectroscopy

Raman spectra were taken of silicon samples by a Renishaw InVia Microscope with a 514 nm source. Each point was integrated over 120 s at 1% laser power with a 600 lines mm^{-1} grating and 2000 cm^{-1} central wavenumber. Three spots were scanned with this configuration on each Si/SiO$_2$ wafer. Raman spectra are arbitrary and cannot be directly compared by intensity between graphs, only by ratio of intensities. A higher I_D/I_G ratio indicated greater defect or pore presence in samples.
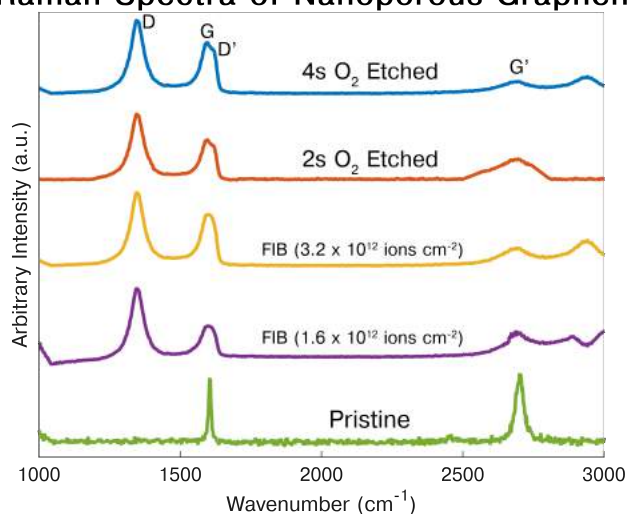

Figure 8. Averaged Raman spectra of pristine and nanoporous graphene on silicon wafers. Only G (~1600 cm^{-1}) and G' (~2700 cm^{-1}) peaks were found in pristine graphene, where as the intensities of D (~1350 cm^{-1}) and D' (~1620 cm^{-1}) peaks were significant in nanoporous graphene. I_D/I_G ratios were 1.92, 1.36, 1.52, 1.39 and 0.24 for graphene samples from top to bottom on the graph.

X-ray Photoelectron Spectroscopy

Electron spectroscopy for chemical analysis (ESCA), or XPS, was applied with a Surface Sciences Instruments M-Probe on three silicon wafer substrates: with pristine, FIB bombarded at 1.6×10^{12} ions cm^{-2} and 4 s O$_2$ plasma-etched graphene. The XPS spectra were collected with a 400 µm spot size, integrated over 4 scans, and at a 45° angle of incidence. A high resolution scan was taken for the pristine graphene sample. Spectra peaks in bombarded and plasma etched graphene sheets indicate presence of C−O, C=O and C−OH bonds, likely in ketone, quinone, hydroxyl or carboxyl functional groups[43–45], as well as C−C and C−H bonds.
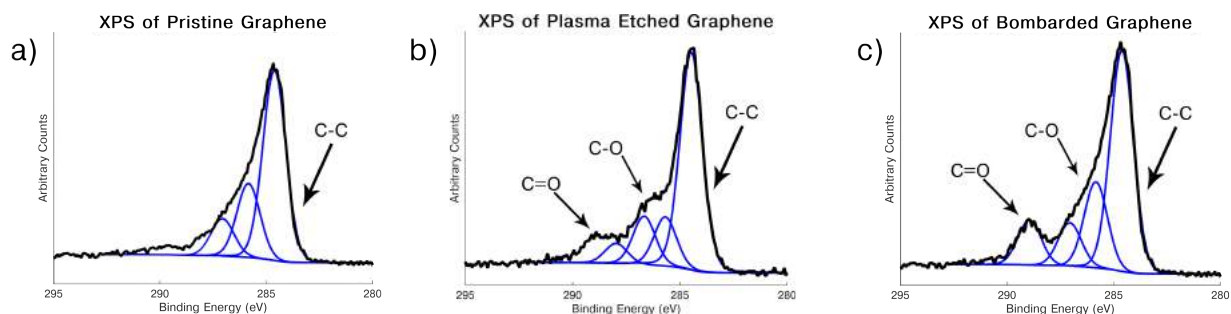

Figure 9. XPS spectra of graphene on silicon that shows formation of carbon and oxygen bonds during plasma and oxidative etching.

Water Transport and Salt Rejection Measurements

To determine experimental permeability and salt rejection of NPG samples, transport measurements were taken of water filtration across pristine, plasma-treated and bombarded graphene single and double layers on PCTEM. A container filled with 500 mL water and 1 M KCl was funneled directly across the 1 cm^2 area of graphene on PCTEM in an oven at 40 °C. Permeate water was collected in an enclosed container and time was measured for filtration of 400 mL of water. To determine ionic rejection, conductivities of the initial feed solution and collected permeate solution at the end of each trial were measured by a Vernier conductivity probe with a National Instruments CompactDAQ and compared. Trials were repeated thrice per graphene sample on PCTEM, as well as through bare PCTEM as a control.

The total driving pressure of feed water in filtration is caused by gravitational forces, its osmotic and vapor pressures and air expansion exclusive of vapor pressure in the oven[24]. The total mass of feed and permeate water solutions were compared between the beginning and end of the trial to determine evaporation and changes in osmotic and vapor pressures across trials. The resultant total driving pressure was found to be ~60 kPa. Few PCTEM with large bare areas found during SEM imagery in the graphene-covered regions were not used and the interface between the funnel and PCTEM were sealed by epoxy, so pathways for water and ionic transport were only across graphene pores that overlapped the 200 nm substrate holes.

The initial conductivity of the feed body was $15.8\,\Omega^{-1}$ (S cm^{-1}) and water per trial across bare PCTEM resulted in a conductivity of $15\,\Omega^{-1}$. Since conductivity is proportional to concentration, the salt rejection was found as a percentage from conductivity of permeate water across graphene out of that across bare PCTEM. The upper limit of conductivity for graphene structures to be suitable for desalination was $0.135\,\Omega^{-1}$, as this corresponds with the 99.1% salt rejection threshold.

Ionic Conductivity Measurements
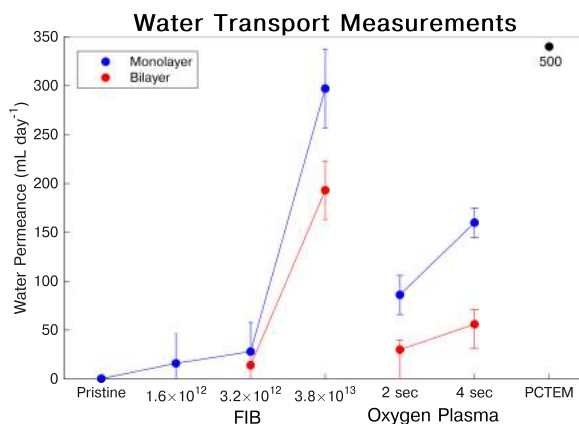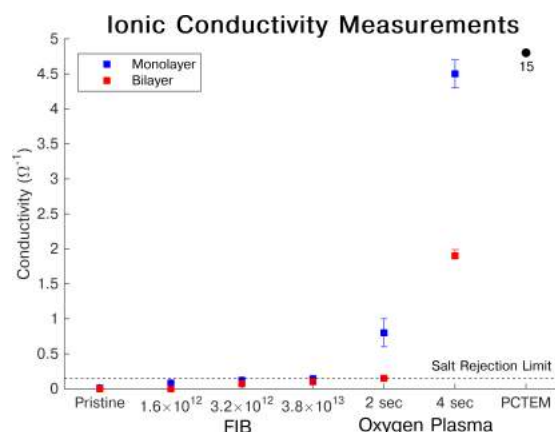
The FIB-bombarded PCTEM demonstrated the highest filtration of 297 mL on average in the one day trials and average conductivity of $0.13\,\Omega^{-1}$. At the applied pressures, this corresponds to a permeability of $4.94\,\mathrm{L\,d^{-1}\,cm^{-2}\,MPa^{-1}}$ and a 99.6% salt rejection rate.

Discussion

Determining optimal structures of nanoporous graphene for desalination is very important for their experimental tuning in laboratory-scales and is thus investigated in this study. First molecular dynamics simulations are applied to determine the optimal structure and then nanopore fabrication methods are experimentally applied to validate these findings.

Previously, molecular dynamics studies have been employed to investigate water flux across single, sub-nanometer pores in graphene sheets[46] and their solute rejection potential according to variable pore sizes and pressures[11]. Other studies find selective rejection of solvated ions from modification of pore chemistries and terminal groups[15]. This work conducts MD simulations, under similar parameters to remain realistic and comparable, but rather investigates membrane-wide effects of multiple pores and increasing pore density in relationship with desalination performance.

These simulations and trials exceed results of previous studies by 1.85 times as hydroxylated pores of adequate size continue to outperform commercial desalination membranes in water permeability, while still rejecting enough salt to produce fresh water. The hydroxylated pores of maximal feasible area, $0.28\,\mathrm{nm^2}$, performed 1.85 times better in permeability than the hydrogenated pores did.

In this investigation, nanoporous graphene bombarded at $3.8 \times 10^{13}\,\mathrm{ions\,cm^{-2}}$, which has a density of $1.2 \times 10^{13}\,\mathrm{pores\,cm^{-2}}$, demonstrates a permeability of $4.94\,\mathrm{L\,d^{-1}\,cm^{-2}\,MPa^{-1}}$ across PCTEM with 10% open area. This indicates that the graphene sheet itself has a higher permeability of approximately $50\,\mathrm{L\,d^{-1}\,cm^{-2}\,MPa^{-1}}$. The experimental study therefore corroborates NPG's theoretical permeability of $53.8\,\mathrm{L\,d^{-1}\,cm^{-2}\,MPa^{-1}}$ offered by molecular dynamic simulations at this density by ~92%. The larger area NPG was likely able to surpass the performance of 1 cm x 1 cm graphene as defect sealing was more intensive over smaller areas and it is easier to handle, although more difficult to grow. Few research groups have fabricated physical graphene for investigation of water and solute fluxes. Nanoporous graphene has previously only proven capability for desalination over an extremely limited continuous area of $7.5 \times 10^{-7}\,\mathrm{cm^2}$[24]. Prior research has been primarily limited by presence of grain boundaries and defects in graphene, as well as by ability to only achieve moderate pore densities[21]. Although this is no longer a limitation due to application of defect-sealing approaches, high pore densities can be achieved by FIB and larger areas can be treated, the bombardment is still resource intensive and time consuming.

The pore fabrication method of oxygen plasma etching has proven effective in small areas[24], but in this study, only the bilayer NPG was able to prevent salt filtration, although plasma-etched samples showed higher permeability than their bombarded counterparts at the same densities. These are likely results of the larger and less controlled pore sizes created from this method. Furthermore, the pore densities are limited to less than 1×10^{13} without extensive damage to graphene by this approach. Bilayer graphene had shown greater salt rejection, but had typically been lower in water permeability. Raman spectroscopy showed defect presence by pore growth methods as expected and XPS demonstrated presence of hydroxyl functional linings, as desired for higher filtration rates.

Though the performance of NPG is on the scale of hundreds of times greater than commercial membranes, only a 27.8% improvement can be expected in energy savings[47], as RO plants already operate at minimum required pressures, which are high and range from 5.5 MPa to $8.0\,\mathrm{MPa}$[2]. Including pre- and post- treatment, actual energy savings should be around 18.5%. Still, at energy costs of $0.10\,\mathrm{kWh^{-1}}$, this reduction would equate to a savings of 6.89 cents $\mathrm{m^{-3}}$ of desalinated water. Thus, in the typical desalination plant, producing $100\,000\,\mathrm{m^3\,d^{-1}}$ of clean water, implementation of NPG membranes could create a daily

energy savings of more than \$6,890. Furthermore, many RO plants utilize tens of thousands of these expensive membrane pressure vessels and this implementation can also reduce the quantity of necessary pressure vessels by 65%. As a result, the implementation of NPG as a membrane in commercial desalination provides even greater incentive in reduction of material and capital costs as well as energy production[48].

Method of synthesis for NPG membranes is also important, as it affects the electronic properties of the membrane relevant to desalination[11]. Chemical vapor deposition (CVD), rather mechanical exfoliation, is a method that can produce membranes with electronically preferable properties[49]. CVD is a slower process and is dependent on advances in materials science & engineering (MSE), guided by computational methods, before synthesis of many large desalination sheets; however, 80 cm graphene films have already been created from roll-to-roll production[50].

Reverse osmosis is the primary method for desalination and advances in RO membrane technology are essential to make it more economically feasible for provision of clean water in developing nations. Previous studies have demonstrated insights towards potential for nanomembranes, especially graphene, as highly efficient reverse osmosis membranes. Molecular dynamics simulations were utilized to investigate the effect of porosity on mechanical stability of nanoporous graphene in a desalination system and this investigation was used to determine an optimal value of water permeability that certain structures of NPG membranes could perform at. Several experimental methods were applied to transfer, defect-seal and fabricate nanopores in graphene. Graphene membrane structures were characterized and measured for water transport and salt rejection.

To remain mechanically stable and reject salt at the desired level for desalination, nanoporous graphene membranes may have an upper limit for porosity of 5.11% if pores are lined by hydrogen functional groups and 6.22% if pores are lined by alternating hydroxyl groups. Though the hydroxylated membrane shows a greater value of porosity at this point of salt rejection, general trends indicate that hydroxylated graphene tends to reject fewer salt molecules than hydrogenated graphene at the same porosity. Hydroxylated NPG shows greater rates of water filtration and permeability than hydrogenated membranes. At a certain porosity, the linear trends of water permeability can be compared to find that hydroxylated pore flux is 1.85 times greater than that of pores lined with hydrogen.

With the most optimal NPG structure, in which graphene contains two hydroxylated pores ($d = 0.598$ nm) per area of 9 nm^2, the membrane is at its greatest water permeability while still rejecting more than 99.1% of salt ions. NPG in this structure is capable of 124.4 L cm^{-2} d^{-1} MPa^{-1} in water permeability and can be compared to the performances of commercial membranes. Graphene membranes have the potential for permeability 1.85 times greater than shown by previous studies that also utilize similar water model and thermostat parameters[12], but also nearly 5,180 times as much as commercial TFC and 17.3 times ultrafiltration RO membranes. This graphene pore arrangement may be scaled onto larger sheets than the 3 nm x 3 nm cell in study and corresponds with a pore density of 2.22×10^{13} pores cm^{-2}.

Nanopores have been fabricated in monolayer and bilayer graphene sheets, which were sealed of intrinsic defects and grain boundaries by IP and ALD, by ion bombardment with oxidative etching and oxygen plasma etching. Transmission electron microscopy imagery has confirmed diameters and densities of induced pores, while Raman and x-ray photoelectron spectroscopies have determined the surface structure, composition and chemical bonding in nanoporous graphene. Water and ionic transport measurements determine a graphene membrane's potential in desalination.

Transport measurements indicate that monolayer graphene with nanopores fabricated by ion bombardment and a density of 1.2×10^{13} pores cm^{-2} can have a water permeability of approximately 50 L cm^{-2} MPa^{-1}, while rejecting adequate salt for desalination, and correspond with theoretical results by 92%. This is the highest experimental permeability achieved in graphene for desalination and largest area by several orders of magnitude to date. Methods of pore growth by oxygen plasma and oxidative etching have functionalized pore linings with by hydroxyl groups, creating higher rates of transmembrane filtration. Additionally, bilayer nanoporous graphene membranes were found to be lesser in permeability and pores created from oxygen plasma etching are too large and allow for salt filtration.

Materials science and advances in the study of nanomembranes demonstrate significant improvements in application to desalination. Computational methods, through MD, have revealed this great potential for implementation and experimental methods have been applied to validate these and advance efforts towards large-scale implementation. Nanoporous graphene has proven its potential as a reverse osmosis membrane to significantly reduce expenses associated with desalination, improving access to and provision of clean water for the 2.8 billion people that are limited in its access.

References

1. Water, U. Coping with water scarcity: challenge of the twenty-first century. *Prepared for World Water Day* (2007).

2. Greenlee, L. F., Lawler, D. F., Freeman, B. D., Marrot, B. & Moulin, P. Reverse osmosis desalination: water sources, technology, and today's challenges. *Water research* **43**, 2317–2348 (2009).

3. Watkins, K. *Human Development Report 2006-Beyond scarcity: Power, poverty and the global water crisis* (2006).

4. Water, W. M. *The United Nations World Water Development Report 4: Managing Water under Uncertainty and Risk*, vol. 1 (2012).

5. Petersen, R. J. Composite reverse osmosis and nanofiltration membranes. *Journal of membrane science* **83**, 81–150 (1993).

6. Geise, G. M. *et al.* Water purification by membranes: the role of polymer science. *Journal of Polymer Science Part B: Polymer Physics* **48**, 1685–1718 (2010).

7. Pendergast, M. M. & Hoek, E. M. A review of water treatment membrane nanotechnologies. *Energy & Environmental Science* **4**, 1946–1971 (2011).

8. Marchetti, P., Jimenez Solomon, M. F., Szekely, G. & Livingston, A. G. Molecular separation with organic solvent nanofiltration: a critical review. *Chemical reviews* **114**, 10735–10806 (2014).

9. Aghigh, A. *et al.* Recent advances in utilization of graphene for filtration and desalination of water: A review. *Desalination* **365**, 389–397 (2015).

10. Nicolaï, A., Sumpter, B. G. & Meunier, V. Tunable water desalination across graphene oxide framework membranes. *Physical Chemistry Chemical Physics* **16**, 8646–8654 (2014).

11. Cohen-Tanugi, D. *Nanoporous graphene as a water desalination membrane*. Ph.D. thesis, Massachusetts Institute of Technology, Cambridge MA (2015).

12. Cohen-Tanugi, D. & Grossman, J. C. Water desalination across nanoporous graphene. *Nano letters* **12**, 3602–3608 (2012).

13. O'Hern, S. C. *et al.* Selective ionic transport through tunable subnanometer pores in single-layer graphene membranes. *Nano letters* **14**, 1234–1241 (2014).

14. Koenig, S. P., Wang, L., Pellegrino, J. & Bunch, J. S. Selective molecular sieving through porous graphene. *Nature nanotechnology* **7**, 728–732 (2012).

15. Sint, K., Wang, B. & Král, P. Selective ion passage through functionalized graphene nanopores. *Journal of the American Chemical Society* **130**, 16448–16449 (2008).

16. Li, H. *et al.* Ultrathin, molecular-sieving graphene oxide membranes for selective hydrogen separation. *Science* **342**, 95–98 (2013).

17. Sagle, A. & Freeman, B. Fundamentals of membranes for water treatment. *The future of desalination in Texas* **2**, 137–154 (2004).

18. Heiranian, M., Farimani, A. B. & Aluru, N. R. Water desalination with a single-layer mos2 nanopore. *Nature communications* **6** (2015).

19. Finney, J. L. The water molecule and its interactions: the interaction between theory, modelling, and experiment. *Journal of Molecular Liquids* **90**, 303–312 (2001).

20. Bondi, A. van der waals volumes and radii. *The Journal of physical chemistry* **68**, 441–451 (1964).

21. Huang, L., Zhang, M., Li, C. & Shi, G. Graphene-based membranes for molecular separation. *The journal of physical chemistry letters* **6**, 2806–2815 (2015).

22. Král, P., Vukovic, L., Patra, N., Wang, B. & Titov, A. Control of rotary motion at the nanoscale: Motility, actuation, self-assembly. *Journal of Nanoscience Letters— Volume* **1** (2011).

23. Fischbein, M. D. & Drndić, M. Electron beam nanosculpting of suspended graphene sheets. *Applied Physics Letters* **93**, 113107 (2008).

24. Surwade, S. P. *et al.* Water desalination using nanoporous single-layer graphene. *Nature nanotechnology* **10**, 459–464 (2015).

25. Konatham, D., Yu, J., Ho, T. A. & Striolo, A. Simulation insights for graphene-based water desalination membranes. *Langmuir* **29**, 11884–11897 (2013).

26. Humphrey, W., Dalke, A. & Schulten, K. Vmd: visual molecular dynamics. *Journal of molecular graphics* **14**, 33–38 (1996).

27. Stukowski, A. Visualization and analysis of atomistic simulation data with ovito–the open visualization tool. *Modelling and Simulation in Materials Science and Engineering* **18**, 015012 (2009).

28. Hanwell, M. D. *et al.* Avogadro: an advanced semantic chemical editor, visualization, and analysis platform. *Journal of cheminformatics* **4**, 1 (2012).

29. Beu, T. A. Molecular dynamics simulations of ion transport through carbon nanotubes. i. influence of geometry, ion specificity, and many-body interactions. *The Journal of chemical physics* **132**, 164513 (2010).

30. Mooney, D., Müller-Plathe, F. & Kremer, K. Simulation studies for liquid phenol: properties evaluated and tested over a range of temperatures. *Chemical physics letters* **294**, 135–142 (1998).

31. Müller-Plathe, F. Local structure and dynamics in solvent-swollen polymers. *Macromolecules* **29**, 4782–4791 (1996).

32. Jorgensen, W. L., Chandrasekhar, J., Madura, J. D., Impey, R. W. & Klein, M. L. Comparison of simple potential functions for simulating liquid water. *The Journal of chemical physics* **79**, 926–935 (1983).

33. Joung, I. S. & Cheatham III, T. E. Determination of alkali and halide monovalent ion parameters for use in explicitly solvated biomolecular simulations. *The journal of physical chemistry B* **112**, 9020–9041 (2008).

34. Hoek, E. M., Kim, A. S. & Elimelech, M. Influence of crossflow membrane filter geometry and shear rate on colloidal fouling in reverse osmosis and nanofiltration separations. *Environmental Engineering Science* **19**, 357–372 (2002).

35. Müller, E. A. Purification of water through nanoporous carbon membranes: a molecular simulation viewpoint. *Current Opinion in Chemical Engineering* **2**, 223–228 (2013).

36. Ho, T. A. & Striolo, A. Polarizability effects in molecular dynamics simulations of the graphene-water interface. *The Journal of chemical physics* **138**, 054117 (2013).

37. Plimpton, S. Fast parallel algorithms for short-range molecular dynamics. *Journal of computational physics* **117**, 1–19 (1995).

38. Cohen-Tanugi, D. & Grossman, J. C. Water permeability of nanoporous graphene at realistic pressures for reverse osmosis desalination. *The Journal of chemical physics* **141**, 074704 (2014).

39. Yuan, W., Chen, J. & Shi, G. Nanoporous graphene materials. *Materials Today* **17**, 77–85 (2014).

40. Lehtinen, O., Kotakoski, J., Krasheninnikov, A. & Keinonen, J. Cutting and controlled modification of graphene with ion beams. *Nanotechnology* **22**, 175306 (2011).

41. Cancado, L. *et al.* General equation for the determination of the crystallite size la of nanographite by raman spectroscopy. *Applied Physics Letters* **88**, 163106–163106 (2006).

42. Matthews, M., Pimenta, M., Dresselhaus, G., Dresselhaus, M. & Endo, M. Origin of dispersive effects of the raman d band in carbon materials. *Physical Review B* **59**, R6585 (1999).

43. Kosynkin, D. V. *et al.* Longitudinal unzipping of carbon nanotubes to form graphene nanoribbons. *Nature* **458**, 872–876 (2009).

44. Rangel, N. L., Sotelo, J. C. & Seminario, J. M. Mechanism of carbon nanotubes unzipping into graphene ribbons. *The Journal of chemical physics* **131**, 031105 (2009).

45. Wang, S. *et al.* Optical spectroscopy investigation of the structural and electrical evolution of controllably oxidized graphene by a solution method. *The Journal of Physical Chemistry C* **116**, 10702–10707 (2012).

46. Suk, M. E. & Aluru, N. Water transport through ultrathin graphene. *The Journal of Physical Chemistry Letters* **1**, 1590–1594 (2010).

47. Cohen-Tanugi, D. & Grossman, J. C. Nanoporous graphene as a reverse osmosis membrane: recent insights from theory and simulation. *Desalination* **366**, 59–70 (2015).

48. Wang, E. N. & Karnik, R. Water desalination: Graphene cleans up water. *Nature nanotechnology* **7**, 552–554 (2012).

49. Li, X. *et al.* Large-area synthesis of high-quality and uniform graphene films on copper foils. *Science* **324**, 1312–1314 (2009).

50. Bae, S. *et al.* Roll-to-roll production of 30-inch graphene films for transparent electrodes. *Nature nanotechnology* **5**, 574–578 (2010).

Acknowledgments

Author contributions statement

A.K. designed the methods, conducted the simulations and experiments, analyzed the data, and prepared the manuscript.

Additional information

The author declares no competing financial interests.